

Ultrawideband metamaterial absorber for oblique incidence using characteristic mode analysis

KUN GAO,^{id} XIANGYU CAO,* JUN GAO, TONG LI, HUANHUAN YANG, AND SIJIA LI^{id}

Shaanxi Key Laboratory of Artificially-Structured Functional Materials and Devices, Air Force Engineering University, Xi'an 710051, China

*Corresponding author: xiangyucao@163.com

Received 21 July 2022; revised 4 October 2022; accepted 8 October 2022; posted 11 October 2022 (Doc. ID 470998); published 22 November 2022

An ultrawideband, polarization-insensitive, metamaterial absorber for oblique angle of incidence is presented using characteristic mode analysis. The absorber consists of conductive meander square loops and symmetric bent metallic strips, which are embedded with lumped resistors. With the aid of modal currents and modal weighting coefficients, the positions of the lumped resistors are determined. After that, the equivalent circuit (EC) model and admittance formula are proposed and analyzed to further understand the working principle and ultrawide bandwidth. The proposed absorber measures an absorption bandwidth of 4.3–26.5 GHz (144.1% in fractional bandwidth) for 90% absorptivity under normal incidence. At the oblique angle of incidence of 45°, the bandwidth of 90% absorptivity is still 5.1–21.3 GHz (122.72%) for transverse electric (TE) polarization, and 6.8–29.5 GHz (125.07%) for transverse magnetic (TM) polarization. The good agreement among simulation, measurement, and EC calculation demonstrates the validity of the proposed method and indicates that the method can be applied to other microwave and optical frequency bands. The proposed metamaterial absorber can be widely applied in electromagnetic compatibility, electromagnetic interference, radar stealth, and biomedical detection. © 2022 Chinese Laser Press

<https://doi.org/10.1364/PRJ.470998>

1. INTRODUCTION

The development of electromagnetic (EM) metamaterials provides a broad prospect for manipulating the polarization, amplitude, and phase of electromagnetic waves to achieve multifunctionality [1,2]. Metamaterial absorbers (MMA) are widely used in various fields due to their unique characteristics, such as radar stealth [3,4], electromagnetic interference [5], wireless communication [6], imaging systems [7], and biomedical detection [8,9]. Salisbury screen [10], Jaumann absorber [11], and perfect metamaterial absorber [12], as early successful practices, although limited by narrow bandwidth and relatively large thickness, also explored a feasible technical route for metamaterial absorbers design.

The bandwidth, oblique angle of incidence and profile thickness of MMAs are a pair of contradictions that are difficult to reconcile. Therefore, an appropriate compromise should be taken to achieve satisfactory performance. The introduction of circuit analog absorbers is an excellent scheme, which greatly addresses the above limitations [13]. At the same time, equivalent circuit (EC) theory is also a rapid and effective method to guide the design of wideband and low-profile circuit analog absorbers [14–18]. In Ref. [15], the proposed absorber was composed of a lossy layer and four rotationally symmetric bent metallic strips embedded with two chip resistors. The metallic strips embedded with the resistors generated three resonant

modes, and the current was consumed through the chip resistor in different modes. A quasi-single-layer circuit analog absorber was proposed in Ref. [16], with two square loop arrays embedded with lumped elements printed on the top and bottom of the lossy dielectric. In Ref. [17], the usage intercalated few-layer graphene for the development of an optically tunable absorbing metasurface is proposed. The geometrical parameters of the metasurface are optimized using the EC theory, which achieves an optically controllable absorption in terahertz imaging and photodetection. The introduction of equivalent circuit, input impedance, and current distribution provided great insight into the existence of resonance and broadband. In addition, indium tin oxide [19,20], water [21,22], and graphene [23,24] are also applied to develop metamaterial absorption.

However, most of the research in the literature only focuses on the normal incidence, while the absorption for the oblique angle of incidence urgently needs principal insight and practical application [25–27]. In Ref. [26], a dual-section step-impedance frequency selective surface (DSSI-FSS) absorber was developed for oblique incidence applications, and a transmission line model was proposed for DSSI-FSS absorbers at different incidence angles. It exhibited stable absorption properties for both TE and TM polarizations at incident angles from 0° to 45°. In Ref. [27], a novel absorber was proposed, which consists of a conductive square loop array embedded with lumped

resistors and a wide-angle impedance matching (WAIM) layer. Equivalent circuit and rigorous formula derivations are introduced to gain insight into the deterioration of absorption performance under oblique incidence and effect of the WAIM layer. At an incident angle of 45° , the overlapped bandwidth for TE and TM polarizations is still 110.5%.

It is worth mentioning that the equivalent circuit is incapable of designing complex structures, and the guidance of oblique angle of incidence requires rich experience. The source-free characteristic mode theory (CMT) defines a set of mutually orthogonal modal currents, which provides profound physical insights for the analysis and modification of fundamental mode and higher-order modes [28–30]. It has successfully guided the design of metasurface antennas [31–36] and has been applied in the field of microwave absorption [19,37–41]. In Ref. [35], the CMT based on the surface integral equation formalism is proposed for the analysis of plasmonic nanostructures, which can be utilized in the design and tuning of nanoantenna configurations for specific application. Reference [36] demonstrates the value of CMA-based design insights for antenna engineering and looks forward to new research directions for CMA and antenna research. In Ref. [37], a multimode and broadband absorber was proposed using characteristic mode analysis (CMA), and the underlying modal behavior of the absorber was analyzed to guide the design. In Ref. [38], with the aid of the characteristic modes and characteristic currents, the value of loading resistance could be determined. The equivalent impedance and surface current distribution of the absorber were analyzed to study its working mechanism. The successful practice of CMA provides a reference for microwave absorption. To the authors' knowledge, CMA has not yet investigated the metamaterial absorber for oblique angle of incidence.

In this study, a novel ultrawideband, polarization-independent metamaterial absorber for oblique angle of incidence is proposed. The positions of the lumped resistors are determined using the modal field and modal parameters. The EC and admittance formula are analyzed to further understand the working mechanism and ultrawide bandwidth. The proposed absorber achieves a fractional bandwidth of 144.1% for 90% absorptivity under normal incidence. At the oblique angle of incidence of 45° , the bandwidth of 90% absorptivity still reaches four octaves for TE and TM polarizations. The simulation, measurement, and EC calculation demonstrate the effectiveness and reliability of the proposed method; it is also worth pointing out that the method can be extended to other microwave and optical fields.

2. DESIGN AND ANALYSIS OF THE PROPOSED METAMATERIAL ABSORBER

Figure 1 shows the schematic of the metamaterial absorber structure with an element size of P , including two lossy layers and a bottom metal ground. The upper structure adopts a conductive meandering square loop (E1), and lumped resistors R_1 (marked in red) and R_2 (marked in black) are embedded in the right-angled corners and the middle of the square loop, respectively. The middle structure employs four symmetrically placed bent metallic strips embedded (E2) with lumped resistor R_3 (marked in red) at right-angled corners. The thicknesses of

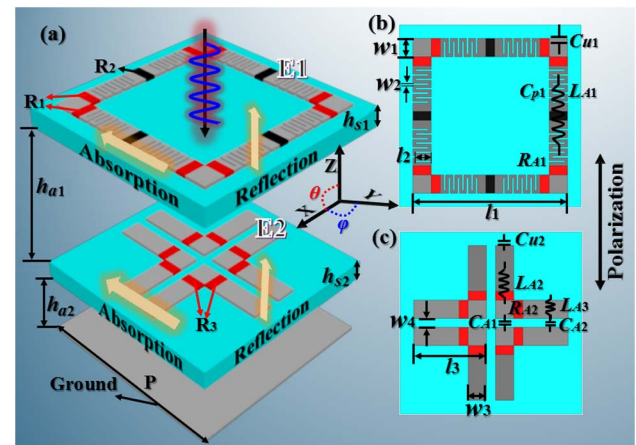


Fig. 1. Topology and dimensions of the proposed metamaterial absorber. (a) Three-dimensional perspective. (b) Top square meander loop embedded with lumped resistors (E1). (c) Middle bent metallic strips embedded with lumped resistors (E2). $P = 10$ mm, $l_1 = 8.5$ mm, $w_1 = 1$ mm, $l_2 = 0.85$ mm, $w_2 = 0.1$ mm, $l_3 = 4$ mm, $w_3 = 1$ mm, $w_4 = 0.5$ mm, $h_{s1} = 0.72$ mm, $h_{s2} = 0.79$ mm, $h_{a1} = 3.8$ mm, and $h_{a2} = 1.5$ mm.

two layers of dielectric substrates are h_{s1} and h_{s2} , respectively, and each layer is filled with air of thickness h_{a1} and h_{a2} , respectively. As shown in Fig. 2, the dielectric constant of the substrate material is 2.65, and, at frequencies above 25 GHz, the dielectric constant is 2.64, which remains stable overall. The dielectric loss is 0.02; at high frequencies, the loss increases slightly. The expression of refractive index is $n_s = \sqrt{\epsilon_r \mu_r}$. Therefore, the refractive index of the substrate material is 1.628 and 1.625 for frequencies above 25 GHz. When the dielectric loss increases, the transmittance decreases and the reflectance increases.

A. Characteristic Mode Analysis and Design of the Absorber

From the characteristic mode theory based on the method of moment (MOM), the radiation and scattering properties of dielectric materials can be clearly obtained [28–30]. The total current J on the conductive surface of different elements can be expressed as a linearly weighted superposition of a series of mutually orthogonal characteristic modes (CMs):

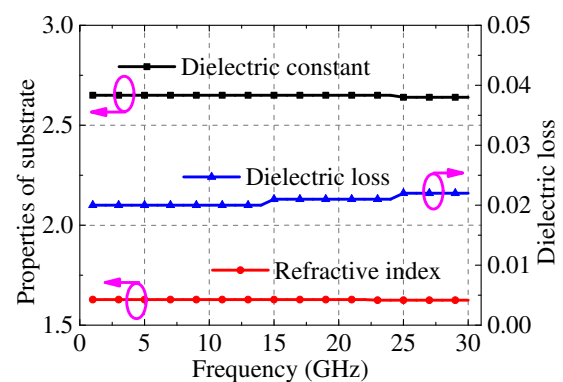


Fig. 2. Properties of substrate.

$$\begin{cases} J_{a,\text{total}} = \sum_n \alpha_{a,n} J_{a,n} \\ J_{b,\text{total}} = \sum_n \alpha_{b,n} J_{b,n} \end{cases} \quad (1)$$

where α_n is the modal weighting coefficient (MWC) of the n th modal current, representing the contribution of each J_n to the total radiated power. The modal weighting coefficient is related to the external electric field and modal current, which is defined as

$$\alpha_n = \frac{\langle E_i(r), J_n \rangle}{1 + j\lambda_n}, \quad (2)$$

where the numerator $\langle E_i(r), J_n \rangle$ is called the modal excitation coefficient. The modal significance (MS) is only related to eigenvalues, expressed as

$$\text{MS} = \left| \frac{1}{1 + j\lambda_n} \right|. \quad (3)$$

The eigenvalue has a large variation range, while the range of MS is [0, 1]. When the value of MS is close to zero, it indicates that the mode is in resonance. If the value of MS is greater than 0.707, it indicates that the mode is an effective mode, which can be effectively excited under appropriate circumstances.

For the absorber, the absorption bandwidth is in the range of MS value greater than 0.707.

The characteristic angle (CA) is expressed as

$$\text{CA}_n = 180^\circ - \arctan \lambda_n. \quad (4)$$

The modes are presented as capacitive for characteristic angles greater than 180° and, on the contrary, exhibit inductance. CMs are obtained using the MOM-based characteristic mode analysis tool in computer simulation technology, Microwave Studio 2020. The dielectric loss is neglected in CMA but considered in the frequency-domain analysis.

The CMA of element 1 (E1) without lumped resistors and meander lines is carried out. Figure 4(a) shows the modal significances, and it can be seen that four dominant modes are resonated within 5–20 GHz. Figures 3(a) and 3(b) show the modal currents and modal radiation patterns of E1. J_{a1} and J_{a2} are a pair of orthogonal modes, and the maximum value of the modal radiation patterns is along the normal direction. The modal current of J_{a3} is the strongest in the middle of each edge, and the modal current of J_{a4} is reversed and rotationally symmetric on each edge. The modal radiation patterns of J_{a3} and J_{a4} are null in the normal direction. The modal currents of J_{a1} , J_{a2} , and J_{a4} are strongest in the right-angled corners. As shown in Figs. 6(a) and 6(c), only J_{a1} and J_{a2} are excited under normally incident

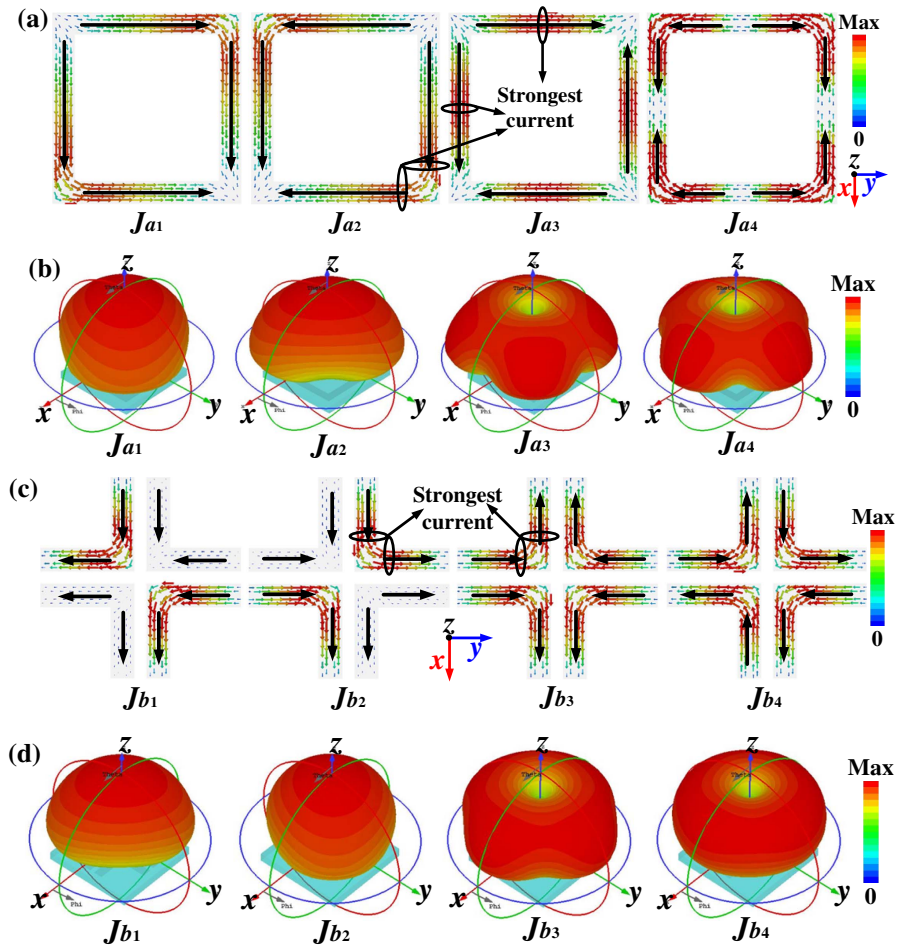


Fig. 3. Modal currents and modal radiation patterns. (a) and (b) Element 1 without lumped resistors and meander lines. (c) and (d) Element 2 without resistors.

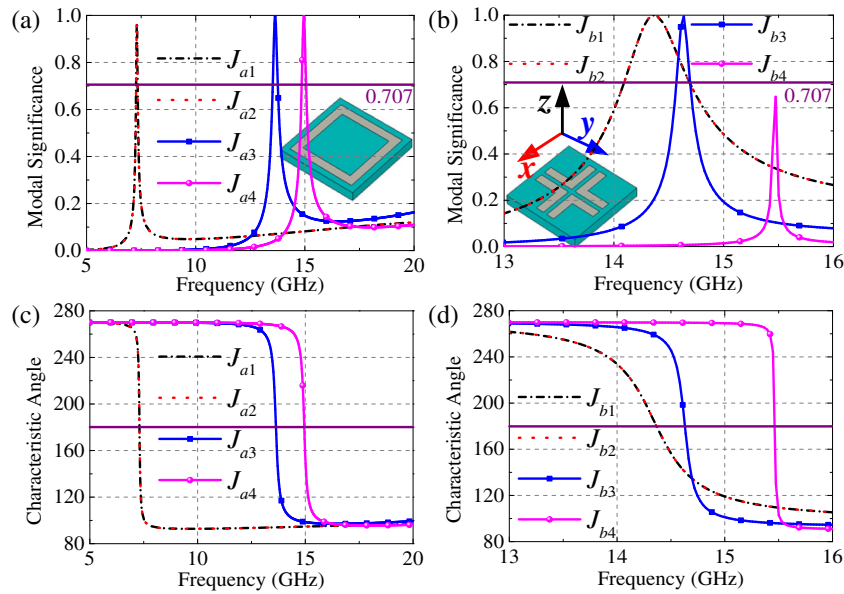


Fig. 4. Modal significances: (a) Element 1 and (b) Element 2 without resistors. Characteristic angles: (c) Element 1 and (d) Element 2 without resistors.

wave. According to the reciprocity theorem, it is evident that the radiation and absorption modes are consistent [42]. Therefore, the modal radiation pattern radiated along the normal direction has the strongest ability to absorb the normally incident wave. For TE polarized incident wave, J_{a1} , J_{a2} (not shown, equal in magnitude to J_{a1}), and J_{a3} are excited. It can be seen that, as the incident angle increases, the excitation of J_{a1} becomes smaller, and the excitation of J_{a3} shifts to high frequency. For TM polarized incidence, J_{a1} and J_{a2} are still the dominant excitation modes. In addition, J_{a4} is also excited.

As the incidence angle increases, the excitation becomes larger and shifts to high frequencies. In order to improve

the absorption capacity of electromagnetic waves under normal incidence and oblique angle of incidence, lumped resistors are loaded at the strongest places of the four modal currents, that is, eight resistors R_1 are loaded at the four corners, and four resistors R_2 are loaded in the middle of each edge. Taking $R_1 = 100 \Omega$ and $R_2 = 100 \Omega$, the CMA is carried out on the E1 loaded with resistance. The modal currents and modal radiation patterns of the four fundamental modes have not changed, but the MS is significantly broadened, as shown in Fig. 5(a). It can be seen from Figs. 4(c) and 5(c) that four dominant modes of E1, with and without the lumped resistors, change from capacitive to inductive. E1 has a sudden mode

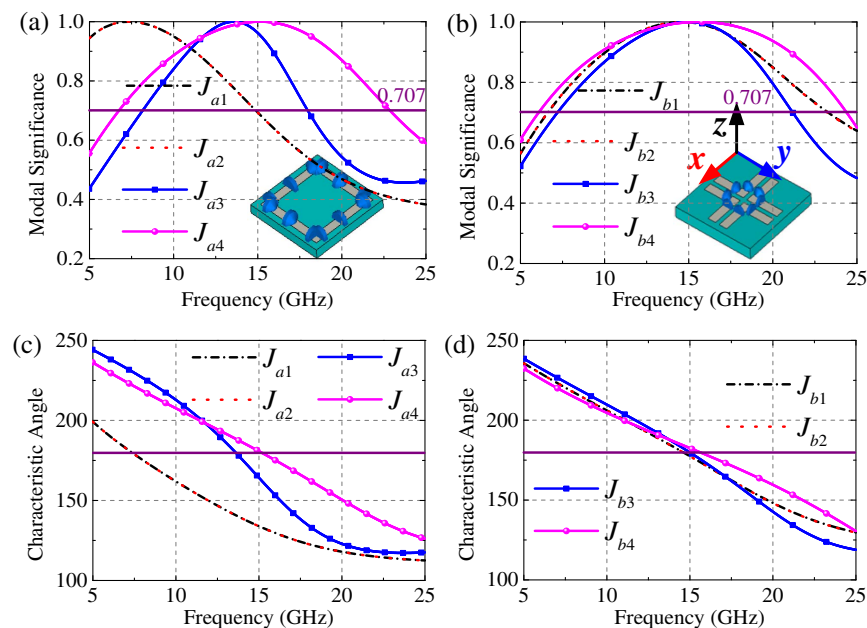


Fig. 5. Modal significances: (a) Element 1 and (b) Element 2 with resistors. Characteristic angles: (c) Element 1 and (d) Element 2 with resistors.

change from capacitive to inductive and a narrow absorption bandwidth when there is no lumped resistor. After loading the lumped resistor, the mode gradually transitions from capacitive to inductive and the absorption bandwidth becomes wider.

Perform the same operation on E2 as E1 and carry out CMA on E2 without resistors to obtain MS. It can be seen that there are also four modes resonating within 13–16 GHz. J_{b1} and J_{b2} are a pair of orthogonal modes, modal radiation patterns all radiate along the normal direction, and there is no doubt that J_{b1} and J_{b2} are mainly excited under the normal incidence. The modal current of J_{b3} is axisymmetric, while the modal current of J_{b4} is rotationally symmetric, and both the modal radiation patterns of J_{b3} and J_{b4} are zero in the normal direction. For TE polarized incident waves, with the increase of incident angle, the excitation of J_{b1} (the excitation of J_{b2} is equal to that of J_{b1} , not shown) becomes smaller, and the excitation of J_{b4} becomes larger, but the amplitude remains relatively smaller. For TE polarized incident waves, with the increase of incident angle, the excitation of J_{b1} (the excitation of J_{b2} is equal to that of J_{b1} , not shown) becomes smaller, and the excitation of J_{b4} becomes larger, but the amplitude remains relatively smaller, as shown in Figs. 6(b) and 6(d). For the TM polarized incident wave, the excitation of J_{b3} is larger as the incident angle increases, and the excitation of J_{b1} increases first and then decreases. At $\theta = 60^\circ$, the excitation of J_{b3} is larger than that of J_{b1} . According to the reciprocity theorem, J_{b1} and J_{b3} play a major role in absorbing waves under oblique angle of incidence [42]. The strongest current of the four modes is located at the corner of the bent metallic strips. In order to expand the bandwidth of MS and enhance the absorption ability under

oblique angle of incidence, lumped resistors are embedded at the strongest modal current. Again, the CMA shows that the modal currents and modal radiation patterns have not changed, and the MS of the four modes has widened, as shown in Fig. 5(b). A strong absorption ability is obtained under normally incident wave and obliquely incident wave. The change process of characteristic angle of E2 is consistent with that of E1.

B. Equivalent Circuit of the Proposed Absorber

Consider the equivalent circuit along the polarization direction of the electric field, as shown in Figs. 1(b) and 1(c). C_{u1} is the coupling capacitance between adjacent E1, L_{A1} is the equivalent inductance on the metallic strip parallel to the polarization direction, C_{p1} is the parasitic capacitance on the metallic strip with the meander line, and the meander line with miniaturized structure is utilized to widen the absorption bandwidth. R_{A1} is the equivalent resistance of R_1 and R_2 inserted into the metallic strip. C_{u2} is the coupling capacitance between adjacent metallic strips in E2, L_{A2} is the equivalent inductance on the metallic strip parallel to the polarization direction, L_{A3} is the equivalent inductance perpendicular to the polarization direction, C_{A1} and C_{A2} are the coupling capacitance between adjacent parallel metallic strips in E2, and R_{A2} is the equivalent resistance of R_3 inserted in the metallic strips. The series resonant circuits $L_{A2}R_{A2}C_{A1}$ and $L_{A3}C_{A2}$ are connected in parallel.

The plane wave is incident on the absorber from free space at θ_1 , and the propagation direction of the electromagnetic wave in the substrate is θ_2 . The incident angle θ_1 and refraction angle θ_2 meet Snell's theorem: $n_1 \sin \theta_1 = n_2 \sin \theta_2$, where $n_1 = \sqrt{\epsilon_0 \mu_0}$ and $n_2 = \sqrt{\epsilon_r \mu_r}$. The admittance of free space and the characteristic admittance of the substrate under normal

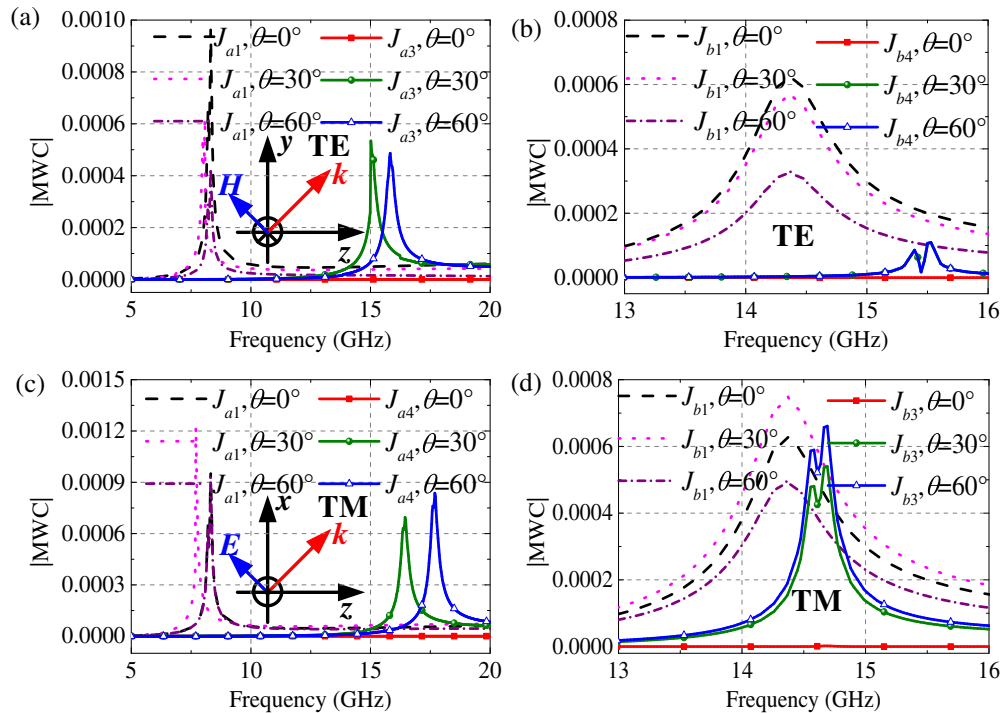


Fig. 6. MWC of Element 1 and Element 2 without resistors at oblique angle of incidence. Element 1 under (a) TE and (c) TM polarization. Element 2 under (b) TE and (d) TM polarization.

incidence are Y_0 , $\sqrt{\epsilon_r/\mu_r}Y_0$, respectively, and under oblique angle of incidence are

$$\begin{cases} Y_0^{\text{TE}} = Y_0 \cos(\theta_1), & Y_0^{\text{TM}} = \frac{Y_0}{\cos(\theta_1)} \\ Y_s^{\text{TE}} = \sqrt{\frac{\epsilon_r}{\mu_r}} Y_0 \cos(\theta_2), & Y_s^{\text{TM}} = \sqrt{\frac{\epsilon_r}{\mu_r}} \frac{Y_0}{\cos(\theta_2)}. \end{cases} \quad (5)$$

Figure 7(a) shows the equivalent circuit model, where Y_{in1} is the input admittance of the proposed absorber. Then, the reflection coefficient is

$$Y_{in1} = Y_s \frac{Y_0 Y_{in2} - Y_s Y_{in2} \tan(\beta_2 h_{s1}) \tan(\beta_1 h_{a1}) + j[Y_0^2 \tan(\beta_1 h_{a1}) + Y_0 Y_s \tan(\beta_2 h_{s1})]}{Y_0 Y_s - Y_0^2 \tan(\beta_2 h_{s1}) \tan(\beta_1 h_{a1}) + j[Y_s Y_{in2} \tan(\beta_1 h_{a1}) + Y_0 Y_{in2} \tan(\beta_2 h_{s1})]} + Y_{RLC1}, \quad (7)$$

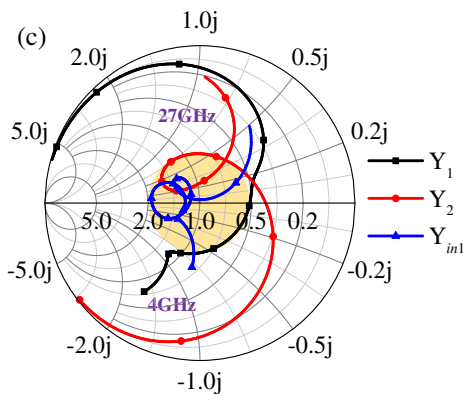
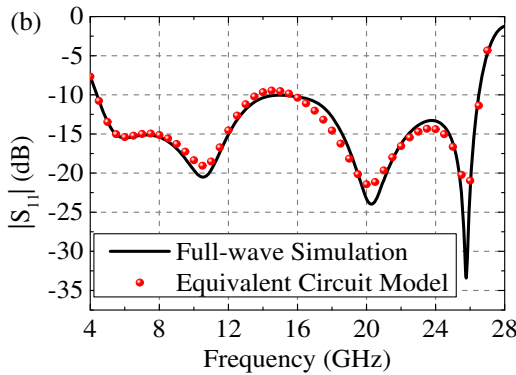
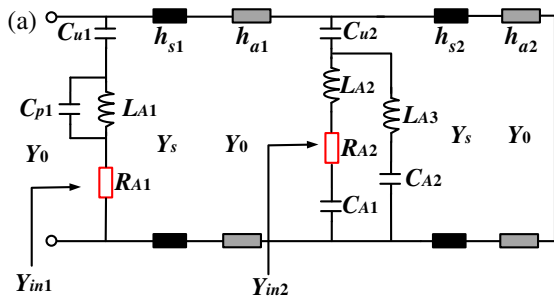


Fig. 7. (a) Equivalent circuit of the proposed absorber. (b) Reflection coefficient of simulation and equivalent circuit model. (c) Admittance Smith chart.

$$\Gamma = \frac{Y_0^{\text{TE,TM}} - Y_{in1}}{Y_0^{\text{TE,TM}} + Y_{in1}}, \quad (6)$$

where Y_{in1} is related to the thickness of free space and substrate and the $R-L-C$ circuit,

$$Y_{RLC1} = \frac{1}{Z_{Cu1} + Z_{RA1} + \frac{Z_{Cp1} Z_{LA1}}{Z_{Cp1} + Z_{LA1}}}, \quad (8)$$

$$Y_{in2} = Y_s \frac{-jY_0 \cot(\beta_1 h_{a2}) + jY_s \tan(\beta_2 h_{s2})}{Y_s + Y_0 \cot(\beta_1 h_{a2}) \tan(\beta_2 h_{s2})} + Y_{RLC2}, \quad (9)$$

$$Y_{RLC2} = \frac{1}{Z_{Cu2} + \frac{(Z_{LA2} + Z_{RA2} + Z_{CA1})(Z_{LA3} + Z_{CA2})}{Z_{LA2} + Z_{RA2} + Z_{CA1} + Z_{LA3} + Z_{CA2}}}, \quad (10)$$

where $\beta_1 = 2\pi \cos(\theta_1)/\lambda$ and $\beta_2 = 2\pi \sqrt{\epsilon_r} \cos(\theta_2)/\lambda$. The known full-wave simulation values are imported into the advanced design system (ADS), and the optimized value with the smallest error from the full-wave simulation value is obtained optimally by the quasi-Newton algorithm in the ADS, which is the desired and optimal $R-L-C$ value. The circuit model is established in the ADS and fitted, and the optimized $R-L-C$ values are $C_{u1} = 0.119$ pF, $L_{A1} = 3.75$ nH, $R_{A1} = 289.7 \Omega$, $C_{p1} = 0.0029$ pF, $C_{u2} = 0.026$ pF, $L_{A2} = 1.778$ nH, $R_{A2} = 230 \Omega$, $C_{A1} = 4.772$ pF, $L_{A3} = 33.22$ nH, and $C_{A2} = 0.001$ pF. The good agreement between the equivalent circuit model and the full-wave simulation demonstrates the reliability of the EC model, as shown in Fig. 7(b). Y_1 and Y_2 are the admittance of single-layer E1 and E2 under the optimal matching state of normally incident wave, respectively. The red shaded area is the -10 dB reflection coefficient. Figure 7(c) shows that the proposed double-layer absorber has a wider absorption bandwidth than the single-layer absorber. After optimization, the resistance values of R_1 , R_2 , and R_3 are 97.6Ω , 97.6Ω , and 73.2Ω , respectively. The absorptivity can be calculated by the following formula:

$$A = 1 - R - T, \quad (11)$$

where $R = |S_{11}|^2$ and $T = |S_{21}|^2$ are the reflectance and transmittance, respectively. The transmittance is close to zero due to the presence of the ground. As shown in Figs. 8(a) and 8(b), the proposed absorber exhibits polarization insensitivity and angular stability. For TE polarization, the absorptivity is almost

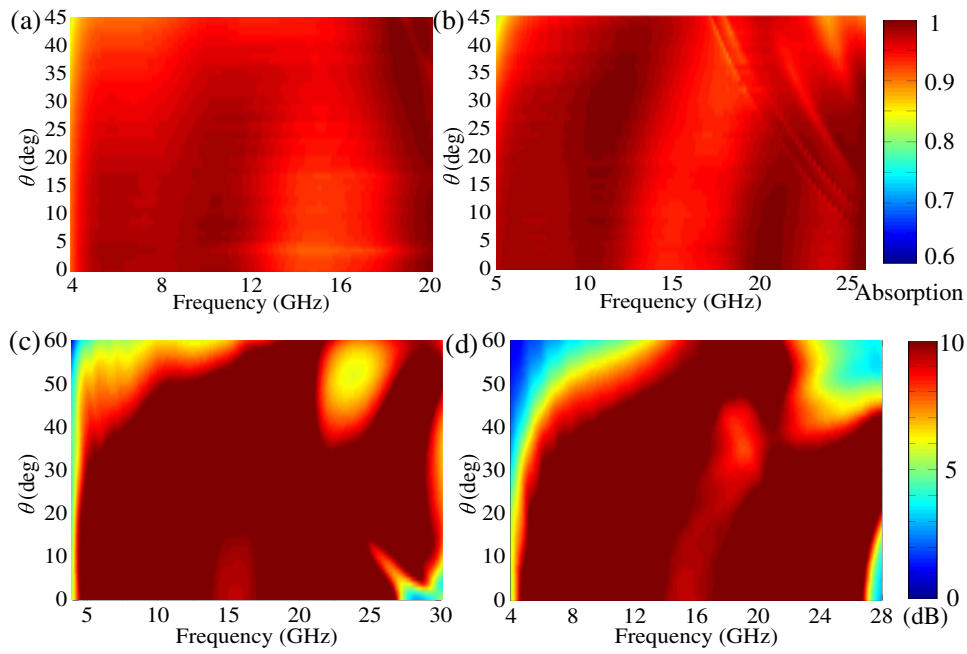


Fig. 8. Simulated absorption variation with incidence angle, for (a) TE and (b) TM polarizations. RCS reduction between the proposed absorber and ground, for (c) TE and (d) TM polarizations.

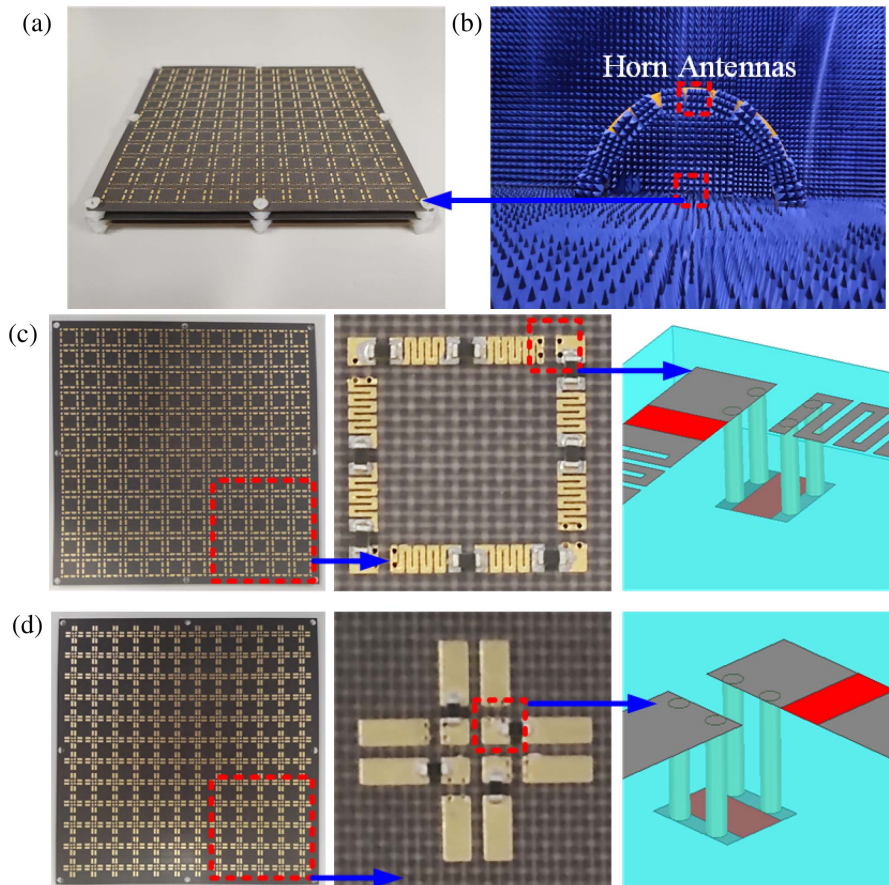


Fig. 9. Fabricated prototypes of absorber array. (a) 3D perspective. (b) Measurement environment. (c) Top layer. (d) Middle layer.

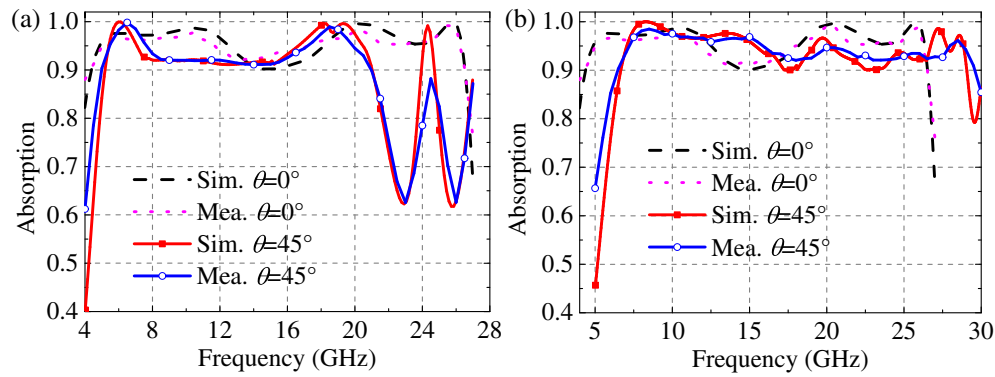


Fig. 10. Simulated and measured absorption for (a) TE polarization and (b) TM polarization.

Table 1. Performance Comparison between the Proposed and Reported Absorbers

Reference	90% Absorption Bandwidth (GHz)	Thickness (λ_L) ^a	Polarization	Angle Absorption	Physical Approach to Absorption	CMA
[15]	2.68–12.19 (127.9%)	0.08	Dual	30° (90%)	Lumped resistors	No
[18]	2.24–11.40 (134.3%)	0.075	Dual	30° (83%)	Lumped resistors	No
[19]	5.51–36.56 (147.6%)	0.117	Dual	40° (80%)	Indium tin oxide	Yes
[26]	2.3–13.3 (144.0%)	0.138	Dual	45° (90%)	Dual-section step-impedance	No
[27]	1.08–5.9 (137.1%)	0.113	Dual	45° (90%)	Wide-angle impedance matching	No
[37]	1–4.5 (127.3%)	0.0883	Dual	N.A.	Resistive film	Yes
[38]	3.21–14.35 (126.88%)	0.098	Dual	45° (85%)	Resistive film	Yes
Proposed	4.3–26.5 (144.1%)	0.097	Dual	45° (90%)	Lumped resistors	Yes

^a λ_L is the wavelength in free space at the lowest operating frequency.

above 90% at 4–20 GHz, except for some frequency bands. For TM polarization, as the incident angle increases, the bandwidth of 90% absorptivity shifts to high frequency, which can still reach four octaves. As shown in Figs. 8(c) and 8(d), compared with the ground with the same area, the proposed absorber can almost be reduced by 10 dB within 0°–60° for TE and TM polarizations. Therefore, the proposed absorber shows excellent performance in absorbing EM waves and reducing the radar cross section (RCS).

3. FABRICATION AND EXPERIMENTS

In order to verify the ultrawideband and polarization-insensitive characteristics of the proposed absorber, an absorber array containing 12×12 elements ($120 \text{ mm} \times 120 \text{ mm}$) is fabricated.

Considering the resistor pads, the space distance between adjacent resistors at the corner is relatively close. Therefore, one of the resistors is placed on the backside of the substrate, connected by metallized vias, as shown in Figs. 9(c) and 9(d). Then, the absorption bandwidth has no effect under normal incidence, and the absorption has little effect under the oblique angle of incidence, except that the absorption bandwidth shifts to low frequency. Figure 10 demonstrates the good agreement between measurements and simulations under TE and TM polarizations. Finally, the absorption bandwidth of the proposed metamaterial absorber for 90% absorptivity is 4.3–26.5 GHz (143.3%) under normal incidence. When the oblique angle of incidence is 45°, the absorption bandwidth under TE polarization and TM polarization is 5.1–21.3 GHz (122.72%)

and 6.8–29.5 GHz (125.07%), respectively. Table 1 shows the performance comparison between the proposed and the previously reported absorbers. It can be seen that the proposed absorber has a wider absorption bandwidth under normal incidence and oblique angle of incidence and has the advantages of simple structure and convenient fabrication.

4. CONCLUSION

This paper presents a novel ultrawideband and dual-polarized metamaterial absorber for oblique angle of incidence. By analyzing the modal fields and parameters, the lumped resistors are loaded at the maximal modal current of the conductive meander square loops and bent metallic strips. At the same time, the equivalent circuit model and the admittance formula are analyzed to further understand the ultrabroadband absorption mechanism. The absorber array is fabricated and measured, and the good agreement between simulation and measurement demonstrates the reliability and effectiveness of the proposed absorber. The bandwidth of 90% absorptivity is 144.1% under normal incidence, and it still reaches four octaves for TE and TM polarizations under oblique incidence of 0°–45°. The proposed metamaterial absorber can be widely applied in electromagnetics, RCS reduction, and biomedical detection. Besides, the proposed method can be extended to other frequency domains and advanced metamaterial absorber designs.

Funding. National Natural Science Foundation of China (62171460); Natural Science Basic Research Program of

Shaanxi Province (2022JM-319, 2022JQ-685, 20210110, 20200108, 20220104, 2020022).

Disclosures. The authors declare no conflicts of interest.

Data Availability. Data underlying the results presented in this paper are not publicly available at this time but may be obtained from the authors upon reasonable request.

REFERENCES

1. T. Cui, "Electromagnetic metamaterials—from effective media to field programmable systems," *Sci. Sin.-Inf.* **50**, 1427–1461 (2020).
2. Z. Vafapour and H. Alaei, "Subwavelength micro-antenna for achieving slow light at microwave wavelengths via electromagnetically induced transparency in 2D metamaterials," *Plasmonics* **12**, 1343–1352 (2017).
3. K. J. Vinoy and R. M. Jha, *Radar Absorbing Materials* (Kluwer, 1996).
4. Z. Zhang, M. Huang, Y. Chen, S.-W. Qu, J. Hu, and S. Yang, "In-band scattering control of ultra-wideband tightly coupled dipole arrays based on polarization-selective metamaterial absorber," *IEEE Trans. Antennas Propag.* **68**, 7927–7936 (2020).
5. P. Zuo, T. Li, M. Wang, H. Zheng, and E.-P. Li, "Miniaturized polarization insensitive metamaterial absorber applied on EMI suppression," *IEEE Access* **8**, 6583–6590 (2020).
6. M. Karaaslan, M. Bağmancı, E. Ünal, O. Akgol, and C. Sabah, "Microwave energy harvesting based on metamaterial absorbers with multi-layered square split rings for wireless communications," *Opt. Commun.* **392**, 31–38 (2017).
7. L. Lei, F. Lou, K. Tao, H. Huang, X. Cheng, and X. Ping, "Tunable and scalable broadband metamaterial absorber involving VO₂-based phase transition," *Photon. Res.* **7**, 734–741 (2019).
8. Z. Vafapour, E. S. Lari, and M. R. Forouzeshefard, "Breast cancer detection capability of a tunable perfect semiconductor absorber: analytical and numerical evaluation," *Opt. Eng.* **60**, 107101 (2021).
9. Z. Vafapour, "Cost-effective bull's eye aperture-style multi-band metamaterial absorber at sub-THz band: design, numerical analysis, and physical interpretation," *Sensors* **22**, 2892 (2022).
10. R. L. Fante, M. T. McCormack, T. D. Syst, and M. A. Wilmington, "Reflection properties of the Salisbury screen," *IEEE Trans. Antennas Propag.* **36**, 1443–1454 (1988).
11. L. J. Du Toit, "The design of Jauman absorbers," *IEEE Antennas Propag. Mag.* **36**, 17–25 (1994).
12. N. I. Landy, S. Sajuyigbe, J. J. Mock, D. R. Smith, and W. J. Padilla, "Perfect metamaterial absorber," *Phys. Rev. Lett.* **100**, 207402 (2008).
13. B. A. Munk, *Frequency Selective Surfaces: Theory and Design* (Wiley, 2000).
14. F. Costa, A. Monorchio, and G. Manara, "Analysis and design of ultra thin electromagnetic absorbers comprising resistively loaded high impedance surfaces," *IEEE Trans. Antennas Propag.* **58**, 1551–1558 (2010).
15. B. Zhang, C. Jin, and Z. Shen, "Low-profile broadband absorber based on multimode resistor-embedded metallic strips," *IEEE Trans. Microw. Theory Tech.* **68**, 835–843 (2020).
16. Y. Shang, Z. Shen, and S. Xiao, "On the design of single-layer circuit analog absorber using double-square-loop array," *IEEE Trans. Antennas Propag.* **61**, 6022–6029 (2013).
17. M. Masyukov, A. N. Grebenchukov, E. A. Litvinov, A. Baldycheva, A. V. Vozianova, and M. K. Khodzitsky, "Photo-tunable terahertz absorber based on intercalated few-layer graphene," *J. Opt.* **22**, 095105 (2020).
18. Z. Yao, S. Xiao, Z. Jiang, L. Yan, and B.-Z. Wang, "On the design of ultrawideband circuit analog absorber based on quasi-single-layer FSS," *IEEE Antennas Wireless Propag. Lett.* **19**, 591–595 (2020).
19. Z. Song, J. Zhu, L. Yang, P. Min, and F. H. Lin, "Wideband metasurface absorber (metabsorber) using characteristic mode analysis," *Opt. Express* **29**, 35387–35399 (2021).
20. Z. Song, P. Min, J. Zhu, L. Yang, and F. H. Lin, "Wideband diffusion metabsorber for perfect scattering field reduction," *Photon. Res.* **10**, 1361–1366 (2022).
21. Y. Chen, K. Chen, D. Zhang, S. Li, Y. Xu, X. Wang, and S. Zhuang, "Ultrabroadband microwave absorber based on 3D water microchannels," *Photon. Res.* **9**, 1391–1396 (2021).
22. J. Xie, S. Quader, F. Xiao, C. He, X. Liang, J. Geng, R. Jin, W. Zhu, and I. D. Rukhlenko, "Truly all-dielectric ultrabroadband metamaterial absorber: water-based and ground-free," *IEEE Antennas Wireless Propag. Lett.* **18**, 536–540 (2019).
23. Y. Fang, K. Pan, T. Leng, H. H. Ouslimani, K. S. Novoselov, and Z. Hu, "Controlling graphene sheet resistance for broadband printable and flexible artificial magnetic conductor-based microwave radar absorber applications," *IEEE Trans. Antennas Propag.* **69**, 8503–8511 (2021).
24. S. Zhong, Y. Zhang, and Y. Ma, "Optically transparent frequency-tunable microwave absorber based on patterned graphene-ITO structure," *IEEE Trans. Antennas Propag.*, in press (2022).
25. B. A. Munk, P. Munk, and J. Pryor, "On designing jaumann and circuit analog absorbers (CA Absorbers) for oblique angle of incidence," *IEEE Trans. Antennas Propag.* **55**, 186–193 (2007).
26. F. He, K. Si, R. Li, D. Zha, J. Dong, L. Miao, S. Bie, and J. Jiang, "Broadband frequency selective surface absorber with dual-section step-impedance matching for oblique incidence applications," *IEEE Trans. Antennas Propag.* **69**, 7647–7657 (2021).
27. Z. Yao, S. Xiao, Y. Li, and B. Wang, "Wide-angle, ultra-wideband, polarization-independent circuit analog absorbers," *IEEE Trans. Antennas Propag.* **70**, 7276–7281 (2022).
28. R. F. Harrington and J. R. Mautz, "Theory of characteristic modes for conducting bodies," *IEEE Trans. Antennas Propag.* **19**, 622–628 (1971).
29. R. F. Harrington, J. R. Mautz, and Y. Chang, "Characteristic modes for dielectric and magnetic bodies," *IEEE Trans. Antennas Propag.* **20**, 194–198 (1972).
30. Y. Chen and C.-F. Wang, *Characteristic Modes: Theory and Applications in Antenna Engineering* (Wiley, 2015).
31. F. H. Lin and Z. N. Chen, "Low-profile wideband metasurface antennas using characteristic mode analysis," *IEEE Trans. Antennas Propag.* **65**, 1706–1713 (2017).
32. F. H. Lin and Z. N. Chen, "A method of suppressing higher-order modes for improving radiation performance of metasurface multipoint antennas using characteristic mode analysis," *IEEE Trans. Antennas Propag.* **66**, 1894–1902 (2018).
33. K. Gao, X. Y. Cao, J. Gao, H. H. Yang, and J. F. Han, "Characteristic mode analysis of wideband high-gain and low-profile metasurface antenna," *Chin. Phys. B* **30**, 064101 (2021).
34. K. Gao, X. Cao, J. Gao, T. Li, H. Yang, and Z. Guo, "Design of a low-RCS circularly polarized metasurface array using characteristic mode analysis," *Opt. Mater. Express* **12**, 907–917 (2022).
35. P. Ylä-Oijala, D. C. Tzarouchis, E. Raninen, and A. Sihvola, "Characteristic mode analysis of plasmonic nanoantennas," *IEEE Trans. Antennas Propag.* **65**, 2165–2172 (2017).
36. J. J. Adams, S. Genovesi, B. Yang, and E. Antonino-Daviu, "Antenna element design using characteristic mode analysis: insights and research directions," *IEEE Antennas Propag. Mag.* **64**, 32–40 (2022).
37. D. Zha, J. Dong, Z. Cao, Y. Zhang, F. He, R. Li, Y. He, L. Miao, S. Bie, and J. Jiang, "A multimode, broadband and all-inkjet-printed absorber using characteristic mode analysis," *Opt. Express* **28**, 8609–8618 (2020).
38. Y. Wu, H. Lin, J. Xiong, J. Hou, R. Zhou, F. Deng, and R. Tang, "A broadband metamaterial absorber design using characteristic modes analysis," *J. Appl. Phys.* **129**, 134902 (2021).
39. Z. Song, P. Min, L. Yang, J. Zhu, and F. H. Lin, "A bilateral coding metabsorber using characteristic mode analysis," *IEEE Antennas Wireless Propag. Lett.* **21**, 1228–1232 (2022).
40. S. Liu, F. Ding, J. Wu, Q. Zhang, and H. Yang, "A metamaterial absorber with centre-spin design and characteristic modes analysis," *Phys. Scr.* **97**, 045502 (2022).
41. H. Chen, Y. Huang, G. Li, Q. He, J. Xie, and L. Deng, "Design and experimental validation of a low-profile wideband metamaterial absorber by characteristic modes analysis," *Results Phys.* **28**, 104684 (2021).
42. T. Shi, M. C. Tang, D. Yi, L. Jin, M. Li, J. Wang, and C. W. Qiu, "Near-omnidirectional broadband metamaterial absorber for TM-polarized wave based on radiation pattern synthesis," *IEEE Trans. Antennas Propag.* **70**, 420–429 (2022).